JACS
JOURNAL OF THE AMERICAN CHEMICAL SOCIETY

ARTICLE

pubs.acs.org/JACS

Simultaneous Large Enhancements in Thermopower and Electrical Conductivity of Bulk Nanostructured Half-Heusler Alloys

Julien P. A. Makongo,[†,§] Dinesh K. Misra,[§] Xiaoyuan Zhou,[‡] Aditya Pant,[§] Michael R. Shabetai,[§] Xianli Su,[‡,#] Ctirad Uher,[‡] Kevin L. Stokes,[§,∥] and Pierre F. P. Poudeu*[,†,§,⊥]

[†]Laboratory for Emerging Energy and Electronic Materials, Materials Science and Engineering Department and [‡]Department of Physics, University of Michigan, Ann Arbor 48109, Michigan, United States

[§]The Advanced Materials Research Institute, [∥]Department of Physics, and [⊥]Department of Chemistry, University of New Orleans, New Orleans, Louisiana 70148, United States

[#]State Key Laboratory of Advanced Technology for Materials Synthesis and Processing, Wuhan University of Technology, Wuhan 430070, China

Supporting Information

ABSTRACT: Large reductions in the thermal conductivity of thermoelectrics using nanostructures have been widely demonstrated. Some enhancements in the thermopower through nanostructuring have also been reported. However, these improvements are generally offset by large drops in the electrical conductivity due to a drastic reduction in the mobility. Here, we show that large enhancements in the thermopower and electrical conductivity of half-Heusler (HH) phases can be achieved simultaneously at high temperatures through coherent insertion of nanometer scale full-Heusler (FH) inclusions within the matrix. The enhancements in the thermopower of the HH/FH nanocomposites arise from drastic reductions in the "effective" carrier concentration around 300 K. Surprisingly, the mobility increases drastically, which compensates for the decrease in the carrier concentration and minimizes the drop in the electrical conductivity. Interestingly, the carrier concentration in HH/FH nanocomposites increases rapidly with temperature, matching that of the HH matrix at high temperatures, whereas the temperature dependence of the mobility significantly deviates from the typical $T^{-\alpha}$ law and slowly decreases (linearly) with rising temperature. This remarkable interplay between the temperature dependence of the carrier concentration and mobility in the nanocomposites results in large increases in the power factor at 775 K. In addition, the embedded FH nanostructures also induce moderate reductions in the thermal conductivity leading to drastic increases in the ZT of HH$(1-x)$/FH(x) nanocomposites at 775 K. By combining transmission electron microscopy and charge transport data, we propose a possible charge carrier scattering mechanism at the HH/FH interfaces leading to the observed anomalous electronic transport in the synthesized HH$(1-x)$/FH(x) nanocomposites.

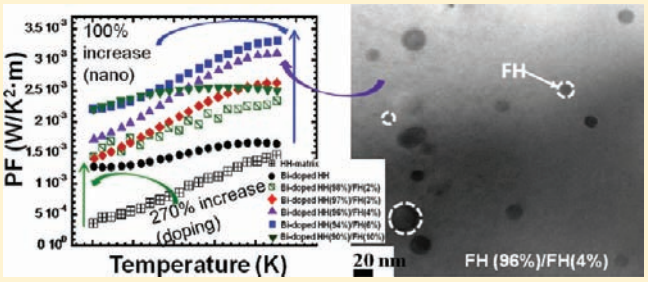

INTRODUCTION

The realization of cost-effective and "clean" solid state energy conversion devices capable of competing with traditional mechanical energy conversion systems requires the ability to fabricate high performance thermoelectric materials with figures of merit, ZT, ≥ 3.[1] Despite substantial increases in research activities and innovative breakthroughs in this area[2−11] over the past six decades, the ability to design thermoelectric materials with ZT approaching the above targeted value has proven extremely difficult mainly because of the interdependence and coupling between electronic and thermal parameters (electrical conductivity, σ; thermopower, S; and thermal conductivity, κ) that enter in the calculation of ZT = $T\sigma S^2/\kappa$. Among various strategies employed to enhance the ZT of traditional and emerging thermoelectric materials, the concept of nanostructuring has drawn much attention primarily due to the prediction that quantum confinement of charge carriers in low dimensional structures within a given matrix could drastically increase ZT of the composite through a large enhancement of the power factor (PF = σS^2).[12,13] Although, the exploration of this concept led to significant increases in the ZT of bulk thermoelectric materials[2,5,6,9,14−21] and thin film superlattices,[11,22] these improvements mainly originate from large reductions in κ rather than an enhancement in the PF as originally predicted. Therefore, the concept of quantum confinement and the mechanism by which nanostructuring can be used to enhance the PF of thermoelectric materials is still poorly understood.

ZT enhancement through large reductions in κ using nanostructuring while minimizing reductions in the PF has therefore dominated thermoelectric research over the past 15 years, and the mechanism by which phonons are scattered at matrix/inclusion

Received: July 12, 2011
Published: October 04, 2011

interfaces is now better understood.[1,23−29] Despite encouraging results obtained through the application of this strategy,[2,5−7,9,11,14−19,30−32] the overall maximum ZT in most material systems (except for the Bi_2Te_3/Sb_2Te_3 superlattices with their ZT ∼2.3 at 300 K) are still below ZT < 2. Further enhancements to reach the targeted goal of ZT ≥ 3 must now come from drastic increases in the PF simultaneously with significant decreases in κ. However, the enhancement in the PF must originate from a dramatic increase in S as opposed to a large increase in σ if the target goal of ZT ≥ 3 is to be achieved. This is due to the fact that by increasing σ, one inevitably increases the electronic part of κ, while an increase in S does not directly affect κ. It is therefore imperative to design and implement innovative concepts that could lead to large enhancements in the PF through (1) drastic increases in S while mitigating losses in σ or (2) significant increase of both S and σ, simultaneously with large reductions in κ.

Among promising thermoelectric materials for power generation, half-Heusler phases with general compositions (Hf,Zr)-NiSn and (Hf,Zr)CoSb have attracted tremendous attention not only because they involve cheap, abundant, lightweight and environmentally friendly elements but also due to their combination of high Seebeck coefficients with moderately low electrical resistivities,[33−39] which give rise to intrinsically high power factors. However, the ability to synthesize half-Heusler based materials with decent figures of merit (ZT > 1) has been jeopardized by their very large thermal conductivities. Current strategies to improve the figures of merit of half-Heusler phases are focusing on the optimization of the PF through substitutional doping and reduction in the thermal conductivity using mass fluctuation phonon scattering via solid-solution alloying[33,37,40] or phonon scattering at grain boundaries in nanometer-sized polycrystalline samples.[40−43] However, the former strategy also induces a large increase in the electronic thermal conductivity, while the latter generally results in a large decrease in the power factor arising from a large reduction in the electrical conductivity.

Here, we introduce the concept of Atomic-Scale Structural Engineering of Thermoelectrics (ASSET) as a new approach to achieve dramatic increases in the PF simultaneously with moderate reductions in κ leading to dramatic enhancements in ZT. We demonstrate using transmission electron microscopy (TEM) and electronic and thermal transport data that ZT values comparable or superior to those reported in single phase half-Heusler systems via traditional doping and substitutional chemistry[40,42,43] can be obtained by embedding coherent well-dispersed sub-10 nm scale fragments of full-Heusler (FH) inclusions within the crystal lattice of a bulk half-Heusler (HH) matrix. We show that this strategy can lead to simultaneous large enhancements of thermopower and electrical conductivity at high temperatures. In addition, we also show that a moderate reduction in the thermal conductivity is achieved simultaneously through enhanced phonon scattering at the sub-10 nm scale matrix/inclusion phase boundaries as well as at grain boundaries. The observed simultaneous large enhancements in both thermopower and electrical conductivity together with a moderate reduction in the total thermal conductivity results in dramatic (up to 250%) improvements of the overall ZT of selected bulk HH/FH nanocomposites. The ability to significantly improve these three parameters simultaneously within a single material system through careful structural engineering at the atomic scale using coherent nanophase boundaries offers excellent opportunities for dramatic further enhancements in the ZT of half-Heusler systems as well as other leading thermoelectric materials.

EXPERIMENTAL SECTION

Synthesis. Polycrystalline powders of $Zr_{0.25}Hf_{0.75}Ni_{1+x}Sn$ (x = 0, 0.02, 0.05), $Zr_{0.25}Hf_{0.75}Ni_{1+x}Sn_{0.975}Bi_{0.025}$ (x = 0, 0.02, 0.03, 0.04, 0.06, 0.10), and $Zr_{0.25}Hf_{0.75}NiSn_{0.975}Sb_{0.025}$ bulk half-Heusler (HH) materials were prepared by direct combination of high purity elements in their powder form at 1173 K for 2 weeks. For each composition, all components, weighed in the appropriate stoichiometric ratio (total mass = 5.0 g), were thoroughly mixed using an agate mortar and pestle under Ar atmosphere and sealed into a silica tube under a residual pressure of $\sim 10^{-4}$ Torr. Another $Zr_{0.25}Hf_{0.75}Ni_{1.02}Sn$ composite was fabricated by reacting approximately 3 g of presynthesized $Zr_{0.25}Hf_{0.75}NiSn$ matrix with 2 atom % excess elemental Ni according to reaction 1.

$$Zr_{0.25}Hf_{0.75}NiSn + 0.02Ni \rightarrow 0.98Zr_{0.25}Hf_{0.75}NiSn\ (HH) + 0.02Zr_{0.25}Hf_{0.75}Ni_2Sn\ (FH) \quad (1)$$

The mixture prepared under inert atmosphere was sealed into a silica tube under a residual pressure of $\sim 10^{-4}$ Torr and then heated for 2 days at 1173 K. Prior to the heat treatment, the mixtures (HH powder and elemental Ni) were milled using a planetary ball mill for 20 min to improve the homogeneity. Products from the $Zr_{0.25}Hf_{0.75}Ni_{1+x}Sn$ and $Zr_{0.25}Hf_{0.75}NiSn_{0.975}Sb_{0.025}$ systems were consolidated by spark plasma sintering (SPS), and samples from the $Zr_{0.25}Hf_{0.75}Ni_{1+x}Sn_{0.975}Bi_{0.025}$ system were densified using a uniaxial hot press (HP). Details of the densification procedures are described elsewhere.[44,45] The relative density of the pellets was obtained by dividing the geometric density (obtained from the pellet mass and dimensions) with the measured density of loose powder (obtained from helium gas pycnometry). Overall, the relative density of the SPS and HP pellets (Table S1 in Supporting Information) were above 92%. The internal structure of selected specimens cut from SPS and HP pellets was examined by transmission electron microscopy (TEM) to probe the size and the distribution of the full-Heusler (FH) nanoinclusions embedded within the HH matrix.

Characterization. The synthesized bulk HH matrices and the resulting HH($1 - x$)/FH(x) nanocomposites were structurally characterized by powder X-ray diffraction using monochromated Cu Kα radiation (λ = 1.54056 Å) on a PANalytical X'pert Pro powder diffractometer operating under 40 kV and 40 mA (Figure S1 in Supporting Information). The electrical conductivity and thermopower of the synthesized HH($1 - x$)/FH(x) nanocomposites were measured simultaneously from 300 to 775 K using a ZEM-3 system from ULVAC-RIKO. The thermal conductivity was calculated from thermal diffusivity and specific heat data measured under flowing N_2 gas (>30 mL/min) using a laser flash apparatus LFA-457 from Netzsch. Carrier density and mobility in the nanocomposites were extracted from Hall coefficients data measured from 300 to 775 K in the magnetic field of ±1 T using a large Oxford air-bore superconducting magnet cryostat that accommodates a small tubular oven and a Hall insert. The Hall signal is monitored with a Linear Research AC Bridge (LR-700) operated at a frequency of 17 Hz.

RESULTS AND DISCUSSION

Generation of Coherent HH/FH Phase Boundaries within a HH Matrix. Nanometer scale coherent phase boundaries in solid matrices can be achieved through a variety of chemical and physical processes, including co-nucleation and growth (intergrowth) during competing chemical reactions, phase segregation during crystal growth from the molten state, phase transformation through solid-state interdiffusion of atoms, or during epitaxial growth. Here, we took advantage of the immiscibility of (Zr,Hf)NiSn (HH) and (Zr,Hf)Ni_2Sn (FH) phases, their three-dimensional structural similarity, and their small lattice

mismatch (~2.5 to 5%) to produce bulk HH(matrix)/FH(inclusion) nanocomposites in a single synthetic step. In these composites sub-10 nm scale FH inclusions of various concentrations, and sizes are confined within the crystal lattice of the semiconducting HH matrix according to the generalized chemical eq 2 (Figure S1 in Supporting Information).

$$z\mathrm{Zr} + (1-z)\mathrm{Hf} + (1+x)\mathrm{Ni} + (1-y)\mathrm{Sn} + y\mathrm{Pn} \rightarrow \mathrm{Zr}_z\mathrm{Hf}_{1-z}\mathrm{Ni}_{1+x}\mathrm{Sn}_{1-y}\mathrm{Pn}_y \quad (\mathrm{HH}(1-x)/\mathrm{FH}(x)) \qquad (2)$$

where Pn = Sb, Bi; $0 \le z, y \le 1$; $0 \le x \le 0.1$ and $Zr_zHf_{1-z}Ni_{1+x}Sn_{1-y}Pn_y$ indicates the $HH(1-x)/FH(x)$ composites with composition $(1-x)Zr_zHf_{1-z}NiSn_{1-y}Pn_y$ (HH) + $xZr_zHf_{1-z}Ni_2Sn_{1-y}Pn_y$ (FH).

The formation of coherent phase boundaries between the HH matrix and the FH inclusion at the sub-10 nm scale is facilitated by the similarity in their crystal structures. Both phases crystallize with face-centered cubic (fcc) structures and feature similar arrangements of (Zr, Hf), Ni, and Sn within the crystal lattice. Therefore, the difference in the formation energy of HH and FH phases with similar chemical compositions should be small. However, they cannot form solid solutions because of the differences in the structure type. HH compounds crystallize in the AgAsMg structure type (space group $F\bar{4}3m$), while FH compounds adopt the $AlCu_2Mn$ structure type (space group $Fm3\bar{m}$). The only structural difference is that half of the tetrahedral sites in the HH structure are vacant. These characteristics are favorable for competing formation of both HH and FH phases when starting from elemental Hf, Zr, and Sn with a small excess of Ni (the Ni excess, x, is calculated on the basis of the stoichiometric HH composition). HH and FH structures could potentially be interchanged without high energy costs (there is only ~2.5% to 5% mismatch on the lattice parameters) through Ni diffusion from the FH sublattice to the vacant sites in the HH sublattice.[45,46] The formation of coherent phase boundaries on the sub-10 nm scale between the HH and FH regions via co-nucleation and growth (intergrowth mechanism) or Ni diffusion into vacant sites in a preformed HH structure (interdiffusion mechanism) is therefore expected. The concentration of FH inclusions in the nanocomposites can be easily controlled through the adjustment of the excess of elemental Ni.[45] However, the size and dispersion of the FH inclusions within the HH matrix are more difficult to control. While some level of control can be achieved by tuning the starting compositions (x values), the size and dispersion of the FH inclusions will have to be altered by the material's synthetic and processing parameters. For this particular study, the absence of the diffraction peaks corresponding to the FH phase on the X-ray diffraction patterns (Figure S1 in Supporting Information) of the synthesized $HH(1-x)/FH(x)$ composites, even for the composite with 10% FH inclusion ($x = 0.1$), suggests that the synthetic method used results in small FH precipitates that do not form aggregates large enough to sharply diffract.

Figure 1A and B shows TEM images of spark plasma sintered (SPS) pellets of $Zr_{0.25}Hf_{0.75}Ni_{1+x}Sn$ ($HH(1-x)/FH(x)$) bulk nanocomposites containing 2 and 5 mol % FH inclusions, respectively. In both composites, spherically shaped nanometer scale precipitates are well dispersed in the HH matrix. The spherical shape of the precipitates suggests their nucleation and isotropic growth as well as their endotaxial insertion within the HH matrix. For the composites with 2 mol % FH ($x = 0.02$), the

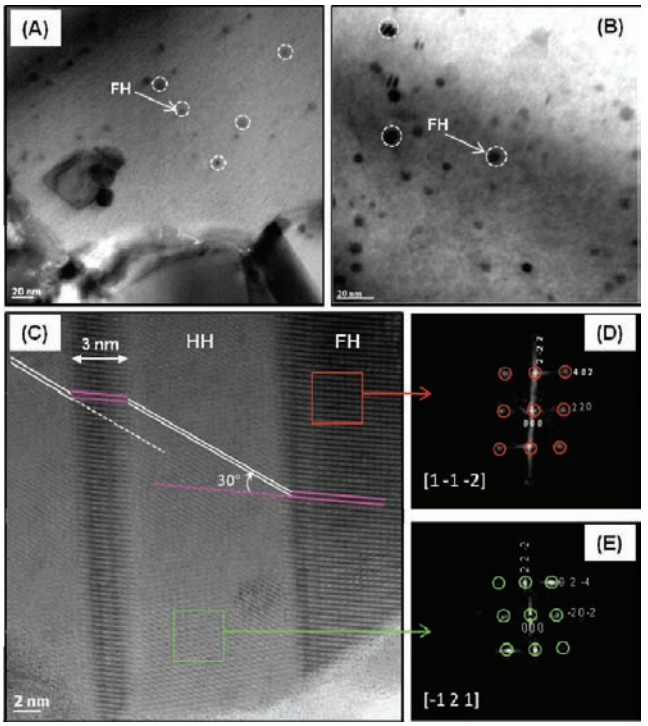

Figure 1. TEM images of spark plasma sintered pellets of $HH(1-x)/FH(x)$ bulk nanocomposites containing 2 mol % (A) and 5 mol % (B) FH inclusions. The spherical shape of the precipitates suggests their nucleation and isotropic growth as well as their endotaxial insertion within the HH matrix. In addition to spherical precipitates, 2−8 nm thick and up to 30 nm long lamellar structures are also observed in panel B. High magnification image of one of the lamellar fine features revealed details of the HH/FH phase boundary structure (C). The FH and HH phases form a tilted coherent interface with tilt angle of approximately $\theta = 30°$. Fast Fourier Transform (FFT) diffractograms of both HH and FH regions showed that the FH inclusions with unit cell parameter $a = 6.29(3)$ Å is oriented along the $[1\bar{1}2]$ zone axis (D), whereas the HH matrix with unit cell parameter $a = 6.06(3)$ Å is oriented along $[\bar{1}21]$ (Figure 1E).

sizes of a large majority of the inclusion phase are on the order of <1 to 3 nm (Figure 1A), although larger precipitates may also be present as well. The formation of such spherical small precipitates with all three dimensions on the order of a few nanometers is reminiscent of quantum dots. Increasing the mole fraction of FH inclusions to 5% ($x = 0.05$) results in higher density and larger size distribution (from ~1 to 20 nm) of the precipitates. In addition to spherical precipitates, 2−8 nm thick and up to 30 nm long lamellar fine features are also observed in samples with 5% FH inclusion (Figure 1B). High magnification imaging of one of the fine lamellar features revealed details of the phase boundary structure (Figure 1C). The precipitates are oriented along a different crystallographic axis with respect to the matrix. Fast Fourier Transform (FFT) diffractograms of both regions (matrix and precipitates) showed that the precipitates are oriented along the $[1\bar{1}2]$ zone axis (Figure 1D), while the HH matrix is oriented along $[\bar{1}21]$ (Figure 1E). The phases form a coherent interface with a tilt angle of approximately 30°. Although the exact chemical composition of the precipitates could not be confirmed, the unit cell parameters of both the precipitates ($a = 6.29(3)$ Å) and the matrix ($a = 6.06(3)$ Å) calculated using FFT diffractograms indicate that the dark-gray precipitates are indeed the FH

phase, while the light-gray matrix is HH (Figure 1C). The nominal composition of the FH according to eq 2, assuming a complete reaction between elements, should be close to $Hf_{0.75}Zr_{0.25}Ni_2Sn$.

Similarly, sub-10 nm scale spherical FH precipitates, well dispersed in micrometer scale grains of the HH matrix, were observed in TEM images of hot pressed (HP) pellets of Bidoped $Zr_{0.25}Hf_{0.75}Ni_{1+x}Sn_{0.975}Bi_{0.025}$ bulk nanocomposites containing 3 and 4 mol % FH inclusions (Figure 2). The spherical FH precipitates with particle sizes ranging from <1 to ~30 nm are coherently embedded in the Bidoped HH matrix. Increasing the mole fraction of FH inclusion (increasing x) results in both broader size range and higher density of the FH inclusions in the HH matrix (Figure 2B and D). The observation of FH precipitates with similar (nanometer scale) sizes in both spark plasma sintered and hot pressed pellets of the synthesized $HH(1-x)/FH(x)$ and Bidoped $HH(1-x)/FH(x)$ nanocomposites suggests that the FH precipitates once formed are stable within the HH matrix and do not grow significantly during processing by SPS or HP.

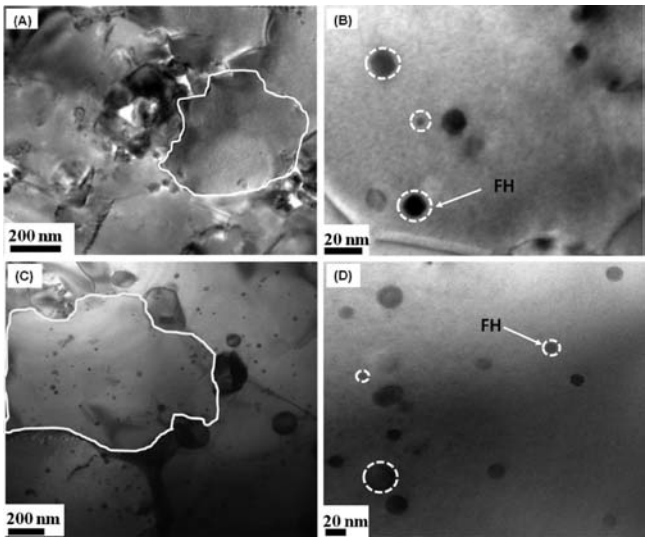

Figure 2. TEM images of hot pressed pellets of the Bidoped $HH(1-x)/FH(x)$ bulk nanocomposites with $x = 0.3$ (A and B) and $x = 0.4$ (C and D). In both samples, nanometer scale particles of the FH inclusion are well dispersed and coherently embedded in micrometer scale grains of the Bidoped HH matrix. Both the size and density of the spherical FH precipitates increase with increasing mole fraction of the FH phase from 3% (B) to 4% (D).

TE Properties of HH/FH Nanocomposites. Figures 3 to 6 show the thermoelectric response of the HH matrix ($Zr_{0.25}Hf_{0.75}NiSn$) and the Bidoped HH matrix ($Zr_{0.25}Hf_{0.75}NiSn_{0.975}Bi_{0.025}$) to the generation of coherent sub-10 nm scale phase boundaries between the HH matrix and the FH inclusion. All samples showed *n*-type semiconducting behavior as indicated by the negative values of the thermopower (Figures 3A and 4A) and Hall coefficient (R_H) (Figures S2A and S4A in Supporting Information). At 300 K, the thermopower of the composite C1 containing 2 mol % FH inclusion (C1 = HH(98%)/FH(2%)) is −252 μV/K (Figure 3A). This represents a 67% increase compared to the value of −148 μV/K measured for the bulk $Hf_{0.75}Zr_{0.25}NiSn$ (HH) matrix and is three times higher than the thermopower of Sb-doped $Hf_{0.75}Zr_{0.25}NiSn_{0.975}Sb_{0.025}$ alloy synthesized and processed under similar conditions. The thermopower for the composite C1 initially increases with temperature reaching a maximum of −290 μV/K at 375 K. Further increases in the temperature result in a slow decrease in the thermopower, and at 775 K, the observed value of −230 μV/K is still ~20% higher than the thermopower of the bulk HH matrix at the same temperature.

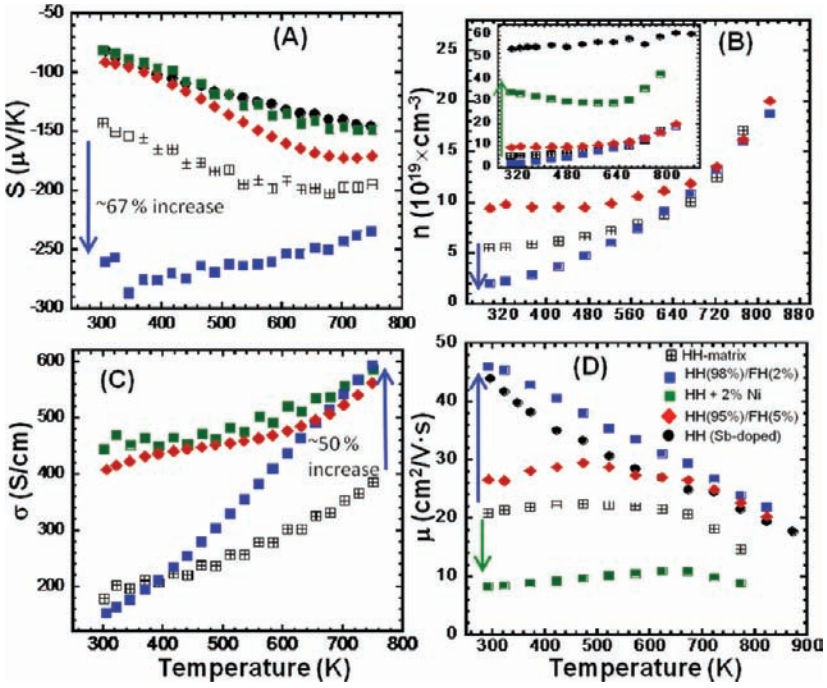

Figure 3. Temperature dependence of the electronic properties of $HH(1-x)/FH(x)$ bulk nanocomposites ($x = 0.02, 0.05$) compared to that of $Zr_{0.25}Hf_{0.75}NiSn$ matrix and Sb-doped and nanostructure-free $Zr_{0.25}Hf_{0.75}NiSn_{0.975}Sb_{0.025}$ bulk half-Heusler alloy: (A) Seebeck coefficient; (B) carrier concentration; (C) electrical conductivity; (D) carrier mobility.

dx.doi.org/10.1021/ja206491j |J. Am. Chem. Soc. 2011, 133, 18843–18852

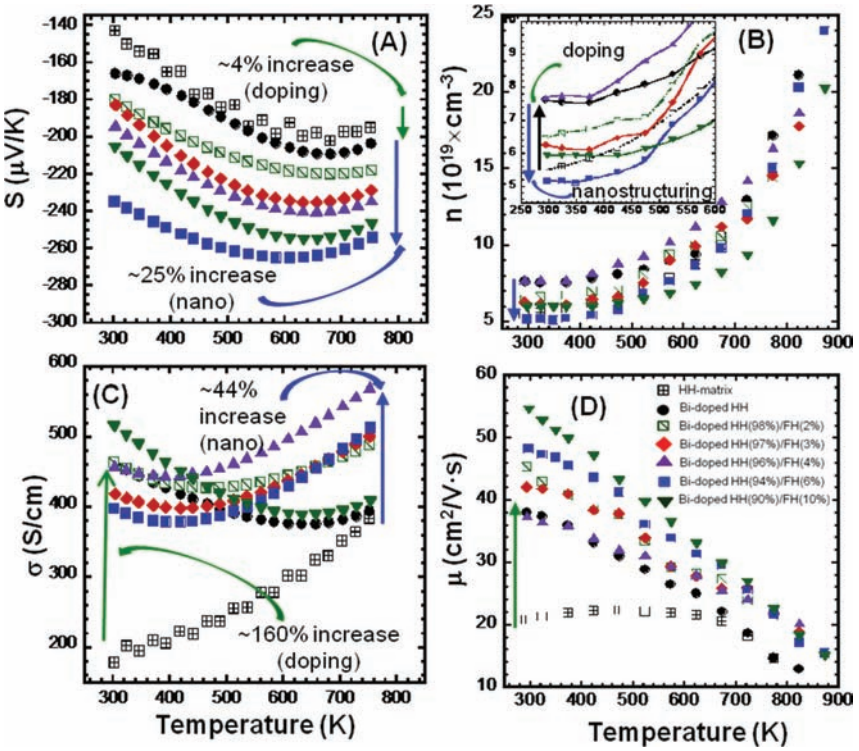

Figure 4. Temperature dependence of the electronic properties of Bidoped HH$(1-x)$/FH(x) $(0 \le x \le 0.1)$ half-Heusler bulk nanocomposites compared to that of undoped $Zr_{0.25}Hf_{0.75}NiSn$ and Bidoped half-Heusler matrix: (A) Seebeck coefficient; (B) carrier concentration; (C) electrical conductivity; (D) carrier mobility.

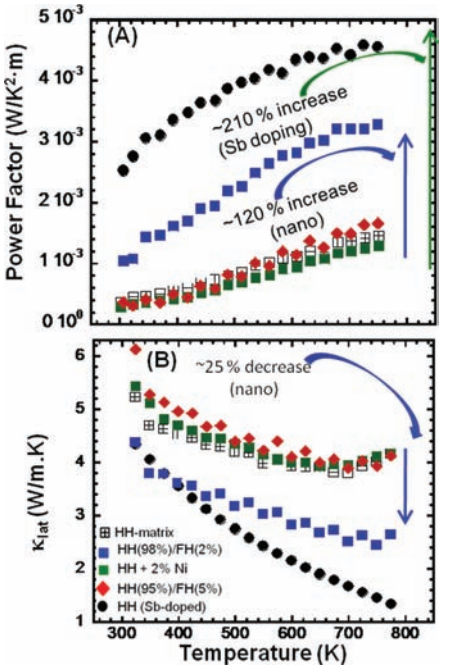

Figure 5. Temperature dependence of the power factor (A) and the lattice thermal conductivity (B) of HH$(1-x)$/FH(x) (x = 0.02, 0.05) half-Heusler bulk nanocomposites compared to that of the $Zr_{0.25}Hf_{0.75}NiSn$ half-Heusler matrix and the Sb-doped $Zr_{0.25}Hf_{0.75}NiSn_{0.975}Sb_{0.025}$ alloy.

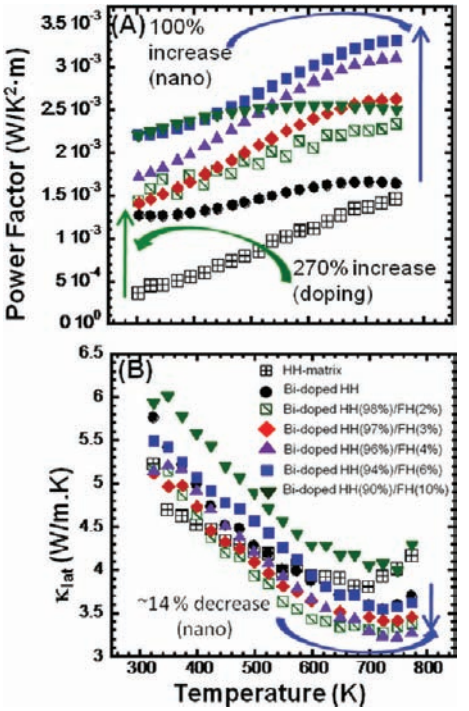

Figure 6. Temperature dependence of the power factor (A) and the lattice thermal conductivity (B) of Bidoped HH$(1-x)$/FH(x) $(0 \le x \le 0.1)$ half-Heusler bulk nanocomposites compared to that of the $Zr_{0.25}Hf_{0.75}NiSn$ half-Heusler matrix.

Similarly, large increases in the thermopower were observed in Bidoped HH/FH nanocomposites (C4−C8). Regardless of the temperature, approximately 4% increase in the thermopower was observed upon doping the $Hf_{0.75}Zr_{0.25}NiSn$ matrix with 2.5% Bi. At 300 K, the thermopower increases from −148 μV/K for the

dx.doi.org/10.1021/ja206491j |J. Am. Chem. Soc. 2011, 133, 18843–18852

undoped HH matrix to −165 μV/K for the Bidoped HH matrix. The introduction of various concentrations of FH inclusions (x = 2%, 3%, 4%, 6% and 10%; Table S1 in Supporting Information) at the nanometer scale in the Bidoped HH matrix resulted in gradual increase in the thermopower of the Bidoped HH$(1-x)$/FH(x) nanocomposites reaching the maximum value for x = 6% (Figure 4A). Further increase in the concentration of FH inclusions to 10% (C8) resulted in lower thermopower values. At 300 K, the highest thermopower value of −235 μV/K was observed for the C7 composite with 6% FH inclusion (C7 = HH(94%)/FH(6%)). This corresponds to ∼42% enhancement of the thermopower, compared to the value measured for the Bidoped HH matrix, and amounts to a 64% increase in the thermopower when compared to the undoped $Hf_{0.75}Zr_{0.25}NiSn$ matrix. Interestingly, the thermopower of the Bidoped HH/FH nanocomposites (C4−C8) monotonically increase with rising temperature, reaching maximum values around 650 K, and decrease thereafter with further increases in temperature. At 775 K, the thermopower of the C7 composite is −255 μV/K, which corresponds to a 28% increase compared to the value of −200 μV/K measured for the Bidoped HH matrix (Figure 4A).

The observed large increases in the thermopower of the nanocomposites (C1, C4−C8) compared to the respective matrices are consistent with the decrease in the carrier densities (n) (Figures 3B and 4B). For instance, a nearly 3-fold reduction (from 5.6×10^{19} cm^{-3} for the HH matrix to 1.9×10^{19} cm^{-3} for C1) in the carrier density was observed at 300 K for the C1 composite (Figure 3B). This is a quite surprising result. Normally, upon introducing metallic FH inclusions within a semiconducting HH matrix, one should expect an increase in the carrier density of the resulting composite if the matrix is doped by the inclusion phase.[45] Otherwise, a carrier density similar to that of the matrix is to be expected if the inclusion is inert with regards to the matrix. We therefore attribute the observed large reduction in the carrier density of the HH/FH nanocomposites around 300 K to the filtering (trapping) of low energy carriers by energy barriers generated at multiple nanometer scale phase boundaries between the HH matrix and the FH inclusions (Figure 7). For the C8 = HH(90%)/FH(10%) composite, a slight increase in the carrier density compared to that of C7 resulted in lower thermopower values. This increase in the carrier density for C8 suggests the presence in the sample of large metallic FH inclusions, which act as dopant for the HH matrix.

Interestingly, the carrier densities in the nanocomposites (C1, C4−C8) increase rapidly with temperature and match those of the respective HH matrices at high temperatures. This behavior strongly suggests that upon increasing the temperature "low energy" electrons from the HH matrix (which were filtered out at around room temperature) gradually gain sufficient thermal energy to allow them to access energy channels through the FH inclusion and therefore also contribute to the electronic transport. However, the observed enhancements in the Seebeck coefficients of the nanocomposites (C1, C4−C8) at high temperatures ($T \geq 600$ K) despite the comparable carrier density with the bulk HH matrices strongly suggests that the distribution of carriers that contribute to the electronic transport are skewed to higher energy (Figure 7), consistent with the energy-dependent electron scattering from metallic inclusions proposed by Faleev and Leonard.[47] In this model, band bending at the metallic inclusion/matrix interfaces induces a potential barrier that acts as an energy filter for low energy electrons, while high energy electrons remain almost unaffected.

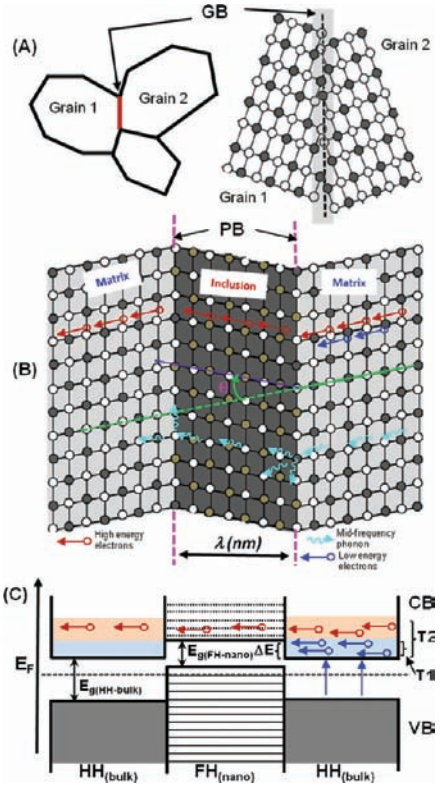

Figure 7. Schematic illustration of examples of atomic scale structural engineering leading to large enhancement of the thermoelectric performance of bulk half-Heusler matrices. (A) Incoherent interface at grain boundaries (BG); (B) coherent phase boundaries (PB) between matrix and inclusion phases with similar structure, which allow close crystallographic registry between both regions; (C) nanometer scale heterojunction between bulk HH matrix and nanometer scale FH inclusion highlighting the proposed low energy electrons filtering mechanism. The conduction band offset, ΔE, is a critical parameter for simultaneous large increase in both Seebeck coefficient and electrical conductivity through filtering of low energy electrons. Cyan and orange colors represent distributions of low and high energy electrons at temperatures T1 and T2 (T2 > T1).

Increasing the concentration of FH inclusions to 5 mol % in the undoped $Zr_{0.25}Hf_{0.75}NiSn$ matrix (C2 = HH(95%)/FH(5%)) resulted in a sharp decrease in thermopower over the whole measured temperature range. At 300 K, the thermopower of the C2 composite is −90 μV/K and increases with temperature to approximately −150 μV/K at 775 K. Comparable values of the thermopower were obtained for another composite C3 = HH(98%)/FH(2%), similar in composition to C1 but prepared through an interdiffusion mechanism by reacting polycrystalline micrometer-sized powders of a presynthesized $Zr_{0.25}Hf_{0.75}NiSn$ HH matrix with excess micrometer-sized powder of elemental Ni (see Experimental Section). The observed large decrease in the thermopower of both C2 and C3 composites originates from an increase in the overall carrier density compared to the HH matrix (inset Figure 3B). This increase in the carrier density for C2 and C3 composites suggests electronic doping of the HH matrix as would be normally expected when metallic inclusions (FH) with sufficiently large size are embedded in a bulk HH matrix.[45,46] This hypothesis is supported by the similarity in the thermopower values for both the C2 and C3 composites with that of the Sb-doped HH alloy with composition $Zr_{0.25}Hf_{0.75}NiSn_{0.975}Sb_{0.025}$ (Figure 3A).

The observed drastic increase in the carrier density of the C2 and C3 composites arising from a small variation of the mole fraction (x) of the FH inclusion phase or a change in the synthetic method strongly suggests that the size and dispersion of the FH inclusion within the HH matrix play a crucial role in the ability to drastically increase the thermopower of HH$(1-x)$/FH(x) nanocomposites through a low-energy electron filtering approach.

The most surprising but yet very interesting finding in this study is the observed large increase at high temperatures in the electrical conductivity of HH$(1-x)$/FH(x) and Bidoped HH$(1-x)$/FH(x) nanocomposites when compared to that of the respective bulk matrices, despite the fact that both the matrix and the resulting nanocomposites have similar carrier densities at high temperatures. Normally, by introducing nanoinclusions in a bulk semiconducting matrix, a drop in the mobility is expected, as each inclusion becomes a scattering center for charge carriers. Therefore, lower electrical conductivity is expected for the HH$(1-x)$/FH(x) and Bidoped HH$(1-x)$/FH(x) nanocomposites at constant carrier concentration. However, we observed that the electrical conductivity of the C1 composite (2% FH) at 300 K is only ∼11% lower than that of the HH-matrix (Figure 3C) despite the measured large decrease in the carrier densities. Astonishingly, the electrical conductivity rapidly increases with temperature outperforming the bulk HH matrix around 400 K. At 775 K, the electrical conductivity of the C1 composite is ∼50% higher than that of the HH matrix (Figure 3C).

Similar behavior of the electrical conductivity was also observed in the Bidoped series of HH$(1-x)$/FH(x) nanocomposites. Upon doping the HH matrix with 2.5% Bi, the room temperature value of the electrical conductivity drastically increases from 200 S/cm for undoped HH to 450 S/cm (160% enhancement) for Bidoped HH matrix (Figure 4C). In addition, the conduction type within the Bidoped HH matrix changes from the intrinsic semiconducting behavior observed for the undoped HH matrix to a heavily doped semiconducting behavior. This behavior is consistent with previous studies on Bidoped HH compounds.[48] The introduction of various concentrations (x) of FH inclusions at the nanometer scale in the Bidoped HH matrix resulted in almost constant values of the electrical conductivity at temperatures below 400 K for the composites C4 (x = 2%) and C6 (x = 4%) and only marginal (13%) loss in the electrical conductivity for C5 (x = 3%) and C7 (x = 6%), despite the observed reduction in the carrier density (Figure 4B). The electrical conductivities of the Bidoped nanocomposites (C4−C7) show two different types of conducting behavior depending on the temperature range. Below 400 K, the electrical conductivity decreases with increasing temperature (typical behavior for heavily doped semiconductor), while a sharp increase in the electrical conductivity with temperature is observed above 400 K (consistent with intrinsic semiconducting behavior). At high temperatures, the electrical conductivities of the Bidoped series of HH$(1-x)$/FH(x) nanocomposites (except for C8 composite) are 30−44% higher than that of the Bidoped HH matrix at 775 K. The composite C8 with 10 mol % FH showed the typical behavior for heavily doped semiconductor over the whole temperature range, presumably due to simultaneous increases in electron mobility and carrier density. This increase in carrier density again suggests partial doping of the HH matrix by FH inclusions with larger size present in C8 composite.

The observed marginal decreases in the electrical conductivity of the C1 and C4−C7 nanocomposites at 300 K results from the fact that the reduction in carrier density arising from the filtering of low energy electrons at the HH/FH interfaces is compensated by a drastic increase in the carrier mobility (Figures 3D and 4D). This surprising increase in the mobility in turn presumably results from the reduction in the frequency of electron−electron collision arising from the large decrease in the "effective" carrier density around 300 K. Interestingly, although the carrier concentrations within the composites increase almost exponentially with temperature and match that of the respective bulk matrices at high temperatures, the temperature dependence of the carrier mobility significantly deviates from the typical $T^{-\alpha}$ law and slowly decreases (linearly) with rising temperature. At 775 K, the carrier mobilities in the nanocomposites (C1, C4−C7) are 80% higher than that of the respective HH matrices. This large difference in the magnitude and the temperature dependence of the mobilities for the synthesized nanocomposites compared to those of the matrices is responsible for the observed enhancements (up to 50%) in the electrical conductivities at high temperatures. A possible charge carrier scattering mechanism responsible for the observed temperature dependence of the carrier concentration and mobility in the synthesized HH/FH nanocomposites is discussed below.

The observed unusual simultaneous increase in thermopower and electrical conductivity for the C1 and C4−C7 nanocomposites at high temperatures results in large increases (up to 120%) in the power factor (PF) at 775 K (Figures 5A and 6A). Although half-Heusler alloys with large power factor can also be achieved through doping strategies and substitutional chemistry, the significance of the observed PF improvement in HH$(1-x)$/FH(x) and Bidoped HH$(1-x)$/FH(x) nanocomposites arises from the fact that it comes from a combination of a large thermopower and moderate electrical conductivity rather than from high electrical conductivity (Figure S2B in Supporting Information) and a small thermopower (Figure 3A) as observed in Sb-doped $Zr_{0.25}Hf_{0.75}NiSn_{0.975}Sb_{0.025}$ alloy.[33] In addition, by combining the Bidoping strategy (which is effective in enhancing the electrical conductivity around room temperatures) with the present atomic scale structural engineering approach (which is effective in enhancing the electrical conductivity at high temperatures), composites with high PF over a broad temperature range were obtained (Figure 6A).

Another remarkable finding in the HH$(1-x)$/FH(x) and Bidoped HH$(1-x)$/FH(x) systems is the fact that in addition to the increase in the power factor, the lattice and total thermal conductivities of the nanocomposites (except for C8) either remain constant or are slightly reduced when compared to those of the respective matrices (Figures 5B, 6B, S3A, and S4B). At 300 K, the lattice thermal conductivity (κ_{lat}) of the C1 composite is 4.4 W/m·K, dropping from 5.1 W/m·K for the undoped $Zr_{0.25}Hf_{0.75}NiSn$ HH matrix. As the temperature increases, κ_{lat} decreases monotonically reaching a value of 2.6 W/m·K at 775K (Figure 5B). This corresponds to a ∼40% reduction in the κ_{lat} of the C1 composite. A similar behavior was observed for κ_{total} of C1 (Figure S3A) with a 25% reduction at high temperatures. Marginal reductions (10% to 14%) in κ_{lat} and κ_{total} were also obtained for the Bidoped nanocomposites (C5 and C7) at 775K (Figure 6B and Figure S4B in Supporting Information). The observed reduction in the lattice thermal conductivities of selected HH$(1-x)$/FH(x) and Bidoped HH$(1-x)$/FH(x) nanocomposites is attributed to the ability of multiple coherent nanometer scale HH/FH phase boundaries (Figures 1 and 2) within the nanocomposites to effectively scatter midfrequency

phonons in addition to the typical scattering of mid-to-long wavelength phonons at grain boundaries as well as the scattering of short wavelength phonons by point defects. The C2, C3, and C8 composites in which larger FH inclusions are present showed a marginal increase in the lattice thermal conductivity, which suggests partial contributions from large metallic FH inclusions to the thermal conductivity of the composites. At high temperatures, the lowest lattice thermal conductivity was observed for the Sb-doped and nanostructure "free" $Hf_{0.75}Zr_{0.25}NiSn_{0.975}Sb_{0.025}$ alloy (Figure 5B) and is ascribed to efficient scattering of short wave wavelength phonons by point defects. However, the Sb-doped $Hf_{0.75}Zr_{0.25}NiSn_{0.975}Sb_{0.025}$ alloy also showed the highest total thermal conductivity (Figure S3A in Supporting Information) due to the large electronic contribution (κ_{el}) arising from its high electrical conductivity.

As a result of the simultaneous increase in both thermopower and electrical conductivity and reduction in κ_{total} of selected $HH(1-x)/FH(x)$ nanocomposites, the overall figures of merit drastically increase at high temperatures (Figures S3B and S4C in Supporting Information). At 775 K, a ZT of ~0.7 was obtained for the C1 composite. This corresponds to a 250% enhancement compared to the ZT~ 0.2 for the undoped $Zr_{0.25}Hf_{0.75}NiSn$ HH matrix at the same temperature (Figure S3B in Supporting Information). It is remarkable to see that, starting from the same undoped $Zr_{0.25}Hf_{0.75}NiSn$ HH matrix system, the present "atomic scale structural engineering of thermoelectrics" (ASSET) approach alone can produce undoped nanocomposites with figures of merit comparable or slightly higher than the ZT value of ~0.6 achieved at 775 K in $Zr_{0.25}Hf_{0.75}NiSn_{0.975}Sb_{0.025}$ alloy using the traditional doping strategy.[33,39] Moreover, the ASSET approach can be combined with the electronic doping strategy to achieve materials with larger values of the thermoelectric figures of merit over a broad temperature range. For instance, in the Bidoped $HH(1-x)/FH(x)$ series of sample, a ZT value of ~0.6 was observed for the C7 (Bidoped HH(94%)/FH(6%)) composite (Figure S4C in Supporting Information) at 775 K. This corresponds to a 72% enhancement when compared to Bidoped $Zr_{0.25}Hf_{0.75}NiSn_{0.975}Bi_{0.025}$ matrix and to a 100% increase when compared to the undoped $Zr_{0.25}Hf_{0.75}NiSn$ matrix.

Charge Carrier and Phonon Scattering at Coherent HH/FH Nanophase Boundaries. Grain and phase boundaries introduced through compaction of nanometer-sized polycrystalline samples or via precipitation of inclusion phases with very different crystal structure inside a given bulk matrix are incoherent in the sense that they do not create crystallographic connectivity between regions separated by the boundaries (Figure 7A). Such incoherent grain or phase boundaries are of high interfacial energy and strongly scatter both high and low energy charge carriers as well as mid-to-long wavelength phonons. As a result, Seebeck enhancement arising from this scattering process is generally offset by a large reduction in the electrical conductivity due to low carrier mobility. This minimizes the power factor enhancement leading to marginal increases in the overall figure of merit despite significant reductions in the thermal conductivity. In addition, such grain boundaries, due to their high interfacial energy, are not thermally stable and are more prone to coarsening at high temperatures, leading to potentially long-term degradation of the material's thermoelectric performance.

In contrast to grain boundaries, coherent phase boundaries formed between matrix and inclusion phases with similar crystal structures allow a close crystallographic registry between both regions (Figure 7B). They are of low energy and potentially thermally stable. The crystallographic orientation of the crystal lattice of the inclusion phase is imposed by local energetic conditions within the matrix. Therefore, tilted or aligned coherent phase boundaries can be observed between the matrix and the inclusion phase. These coherent phase boundaries can be manipulated to effectively enhance the Seebeck coefficient of the matrix simultaneously with large reductions in the thermal conductivity without severe losses in the electrical conductivity. The extent of Seebeck enhancement, electrical conductivity loss or gain, and thermal conductivity reduction achievable can strongly depend on parameters such as the diameter (λ/nm) of the inclusion phase, the tilt angle (θ/deg) between atomic planes at the coherent matrix/inclusion phase boundaries, and the density of such phase boundaries in the materials. In addition, the electronic structures of the matrix and the inclusion as well as the relative alignment of the conduction bands in both structures are important parameters to consider. For instance, the formation of well dispersed spherical FH precipitates with diameters on the order of sub-10 nm ($\leq$10 nm) that are coherently embedded in the HH matrix (Figures 1 and 2) are expected to generate a quantum confinement of electrons within the FH inclusion.[26] The resulting size dependence of the bandgap of the FH nanoinclusions induces the formation of nanometer scale heterojunctions between the HH matrix and FH inclusions (Figure 7C). Given the similarity in the atomic distribution in both HH and FH structures and also because of their lattice coherency, heterojunctions with straddling, staggered, or broken gaps can be expected depending on the size of the FH nanoinclusion. Assuming a staggered gap heterojunction at the HH/FH interface, the resulting conduction band energy offset, $\Delta E = E_{(CBM,FH)} - E_{(CBM,HH)}$ (where $E_{(CBM,FH)}$ and $E_{(CBM,HH)}$ are the conduction band minima (CBM) energy in the FH inclusion and HH matrix, respectively), is a critical parameter for simultaneous large increase in both Seebeck coefficient and electrical conductivity through filtering of low energy electrons. ΔE can be engineered by modifying the size and dispersion of the FH inclusion. For a given matrix/inclusion system, the size (λ) of the FH inclusion should be reduced down to the sub-10 nm length scale where quantum confinement effects lead to a bandgap ($E_{g,FH\text{-}nano}$) larger than the conduction band's energy offset, ΔE. In the $Zr_{0.25}Hf_{0.75}Ni_{1+x}Sn$ and $Zr_{0.25}Hf_{0.75}Ni_{1+x}Sn_{0.975}Bi_{0.025}$ systems, this condition is probably achieved for FH inclusions less than 10 nm in diameter (Figures 1 and 2). Under this condition, only high energy electrons ($E \geq E_{(CBM,FH)}$) from the top of the CB of the HH matrix can tunnel through the CB of the FH inclusion (Figure 7C). Low energy electrons ($E < E_{(CBM,FH)}$) at the bottom of the CB of the HH matrix are blocked (trapped), resulting in the observed decrease around 300 K of the "effective" carrier density in the synthesized nanocomposites (Figures 3B and 4B). This decrease in carrier density is believed to be responsible for the large enhancement in the Seebeck coefficient of $Zr_{0.25}Hf_{0.75}Ni_{1+x}Sn$ and $Zr_{0.25}Hf_{0.75}Ni_{1+x}Sn_{0.975}Bi_{0.025}$ nanocomposites. Upon increase in the temperature, the distribution of electrons within the CB of the HH matrix is pushed to higher energy (Figure 7C). In addition more electrons are promoted from the VB to the CB of the HH matrix due to thermal excitation. Low energy electrons that initially (around 300 K) were blocked by the CB band offset, ΔE, can now access energy channels through the FH inclusion ($E \geq E_{(CBM,FH)}$), leading to their contribution to the electronic transport at high temperatures. This mechanism is consistent with the observed nearly

exponential increase in the carrier concentration with temperature (Figures 3B and 4B).

In order to understand the observed unusual increase of the mobility in the synthesized nanocomposites as well as their temperature dependence, one must keep in mind that as a consequence of the filtering of low energy electrons at the HH/FH phase boundaries, the "effective" carrier density around room temperature (below 500 K) is significantly lower than that of the matrix. This implies a reduction in the frequency of electron−electron collisions and/or a reduction in the strength of electron−phonon coupling, leading to a net increase in the mobility. Upon increasing the temperature, the new distribution of low energy (LE) and high energy (HE) electrons within the CB of the HH matrix arising from the electron energy filtering effect causes the observed electron mobility in the nanocomposites at various temperatures to be a complex function of the average electron mobilities within individual subgroups (LE and HE electrons). At a given temperature, high energy electrons tend to have lower mobility compared to low energy ones, mainly because of their high electron−electron and acoustic phonon−electron scattering. Therefore, the overall carrier mobility within the composites at a given temperature strongly depends on the relative concentration of low energy and high energy electrons as well as the average mobility of their subgroup. For a given matrix/inclusion system, the relative fraction of high energy or low energy electrons can be tuned by varying ΔE through the alteration of the size (λ) of the inclusion. For the $Zr_{0.25}Hf_{0.75}Ni_{1+x}Sn$ and $Zr_{0.25}Hf_{0.75}Ni_{1+x}Sn_{0.975}Bi_{0.025}$ nanocomposites reported here, the carrier densities increase exponentially with increasing temperature (Figures 3B and 4B). This suggests that the fraction of low energy electrons (relative to high energy electrons) gradually increases with temperature, leading to the observed slower decrease in the overall carrier mobility within the nanocomposites. The departure of the temperature dependence of the overall mobility from the typical $T^{-\alpha}$ law is therefore achieved by decoupling the temperature dependence of the mobility of low energy and high energy electrons using sub-10 nm scale coherent phase boundaries between the HH matrix and FH inclusions. This anomalous temperature dependence of the overall mobility in the synthesized nanocomposites is responsible for the observed rapid increase in the electrical conductivity at high temperatures (Figures 3C and 4C).

In addition to the large increases in the power factor, the introduction of sub-10 nm scale coherent HH/FH phase boundaries within a HH matrix also leads to large reductions in the lattice thermal conductivity of the nanocomposites. Nanometer scale (<10 nm) inclusion phases are effective in scattering midfrequency phonons (Figure 7B) in addition to the typical scattering of mid-to-long wavelength phonon scattering at grain boundaries. Because the HH matrix and FH inclusion can have different orientations, the formation of coherent tilted (with tilt angle, θ/deg) phase boundaries is possible (Figures 1C and 7B). This structural feature can induce large strains at the HH/FH phase boundaries, which enhance the scattering of midfrequency phonons propagating through the crystal lattice of the matrix. The degree to which midfrequency phonons are scattered by inclusions can be enhanced by tuning the tilt angle (θ/deg) and/or the thickness (λ/nm) of the inclusion. Therefore, optimal values of the tilt angle and the thickness of the inclusion must be obtained to maximize the reduction in the thermal conductivity simultaneously with a dramatic increase in the power factor.

CONCLUSIONS

We have demonstrated that simultaneous large increases in the thermopower and electrical conductivity of HH materials can be achieved at high temperatures through controlled insertion of stable and well-dispersed coherent internal phase boundaries between the bulk HH matrix and nanometer scale FH inclusions. The large increase in the thermopower results from the filtering of low energy electrons at the nanometer scale HH/FH phase boundaries leading to a decrease in the carrier density around room temperature. This reduction in carrier density is compensated by a large increase in the carrier mobility, which minimizes the loss in the electrical conductivity. At high temperatures, the electrical conductivity rapidly increases due to an exponentially increasing carrier density and slow decrease in carrier mobility. This simultaneous increase in thermopower and electrical conductivity at high temperatures leads to spectacular increases in the power factor of the HH/FH nanocomposites. In addition, this "Atomic-Scale Structural Engineering of Thermoelectrics" (ASSET) approach also leads to a moderate reduction in the thermal conductivity due to effective scattering of midfrequency phonons at nanometer scale HH/FH phase boundaries in addition to the typical scattering of mid-to-long wavelength phonons at grain boundaries. The ASSET approach is a general concept, and we anticipate that its successful application to current leading *n*-type and *p*-type half-Heusler and other promising thermoelectric materials will lead to significant further enhancements in their figures of merit at high temperatures.

ASSOCIATED CONTENT

Supporting Information. Supplementary Table S1 and Figures S1−S4. This material is available free of charge via the Internet at http://pubs.acs.org.

AUTHOR INFORMATION

Corresponding Author
ppoudeup@umich.edu

ACKNOWLEDGMENT

The authors gratefully acknowledge financial support from DARPA (contracts no. HR 0011-08-1-0084 and W91CRB-10-C-0189). This work made use of the laser flash diffusivity apparatus (Netzsch-LFA457) purchased with funds from the Louisiana Board of Regents (Grant no. LEQSF(2008-09)-ENH-TR-58). The work at the University of Michigan (high temperature Hall effect measurements) is supported by the Center for Solar and Thermal Energy Conversion, an Energy Frontier Research Center funded by the U.S. Department of Energy, Office of Basic Energy Sciences under Award no. DE-SC0000957. The authors thank Dr. James Salvador from the Chemical Sciences and Materials Systems Laboratory, General Motors R&D Center for assistance in samples consolidation using spark plasma sintering. Patent protection related to this work is pending.

REFERENCES

(1) Vineis, C. J.; Shakouri, A.; Majumdar, A.; Kanatzidis, M. G. *Adv. Mater.* **2010**, *22*, 3970.

(2) Hsu, K. F.; Loo, S.; Guo, F.; Chen, W.; Dyck, J. S.; Uher, C.; Hogan, T.; Polychroniadis, E. K.; Kanatzidis, M. G. *Science* **2004**, *303*, 818.

(3) Heremans, J. P.; Jovovic, V.; Toberer, E. S.; Saramat, A.; Kurosaki, K.; Charoenphakdee, A.; Yamanaka, S.; Snyder, G. J. *Science* **2008**, *321*, 554.
(4) Boukai, A. I.; Bunimovich, Y.; Tahir-Kheli, J.; Yu, J. K.; Goddard, W. A.; Heath, J. R. *Nature* **2008**, *451*, 168.
(5) Poudeu, P. F. P.; D'Angelo, J.; Downey, A. D.; Short, J. L.; Hogan, T. P.; Kanatzidis, M. G. *Angew. Chem., Int. Ed.* **2006**, *45*, 3835.
(6) Androulakis, J.; Hsu, K. F.; Pcionek, R.; Kong, H.; Uher, C.; DAngelo, J. J.; Downey, A.; Hogan, T.; Kanatzidis, M. G. *Adv. Mater.* **2006**, *18*, 1170.
(7) Harman, T. C.; Taylor, P. J.; Walsh, M. P.; LaForge, B. E. *Science* **2002**, *297*, 2229.
(8) Hochbaum, A. I.; Chen, R. K.; Delgado, R. D.; Liang, W. J.; Garnett, E. C.; Najarian, M.; Majumdar, A.; Yang, P. D. *Nature* **2008**, *451*, 163.
(9) Poudel, B.; Hao, Q.; Ma, Y.; Lan, Y. C.; Minnich, A.; Yu, B.; Yan, X.; Wang, D. Z.; Muto, A.; Vashaee, D.; Chen, X. Y.; Liu, J. M.; Dresselhaus, M. S.; Chen, G.; Ren, Z. *Science* **2008**, *320*, 634.
(10) Rhyee, J. S.; Lee, K. H.; Lee, S. M.; Cho, E.; Il Kim, S.; Lee, E.; Kwon, Y. S.; Shim, J. H.; Kotliar, G. *Nature* **2009**, *459*, 965.
(11) Venkatasubramanian, R.; Siivola, E.; Colpitts, T.; O'Quinn, B. *Nature* **2001**, *413*, 597.
(12) Hicks, L. D.; Dresselhaus, M. S. *Phys. Rev. B* **1993**, *47*, 12727.
(13) Hicks, L. D.; Harman, T. C.; Dresselhaus, M. S. *Appl. Phys. Lett.* **1993**, *63*, 3230.
(14) Wang, H.; Li, J. F.; Nan, C. W.; Zhou, M.; Liu, W. S.; Zhang, B. P.; Kita, T. *Appl. Phys. Lett.* **2006**, *88*, 092104.
(15) Poudeu, P. F. P.; Gueguen, A.; Wu, C. I.; Hogan, T.; Kanatzidis, M. G. *Chem. Mater.* **2010**, *22*, 1046.
(16) Gueguen, A.; Poudeu, P. F. P.; Li, C. P.; Moses, S.; Uher, C.; He, J. Q.; Dravid, V.; Paraskevopoulos, K. A.; Kanatzidis, M. G. *Chem. Mater.* **2009**, *21*, 1683.
(17) Androulakis, J.; Lin, C. H.; Kong, H. J.; Uher, C.; Wu, C. I.; Hogan, T.; Cook, B. A.; Caillat, T.; Paraskevopoulos, K. M.; Kanatzidis, M. G. *J. Am. Chem. Soc.* **2007**, *129*, 9780.
(18) Lan, Y. C.; Poudel, B.; Ma, Y.; Wang, D. Z.; Dresselhaus, M. S.; Chen, G.; Ren, Z. F. *Nano Lett.* **2009**, *9*, 1419.
(19) Yan, X.; Joshi, G.; Liu, W.; Lan, Y.; Wang, H.; Lee, S.; Simonson, J. W.; Poon, S. J.; Tritt, T. M.; Chen, G.; Ren, Z. F. *Nano Lett.* **2011**, *11*, 556.
(20) Li, H.; Tang, X.; Zhang, Q.; Uher, C. *Appl. Phys. Lett.* **2009**, *94*, 102114.
(21) Biswas, K.; He, J. Q.; Zhang, Q. C.; Wang, G. Y.; Uher, C.; Dravid, V. P.; Kanatzidis, M. G. *Nat. Chem.* **2011**, *3*, 160.
(22) Caylor, J. C.; Coonley, K.; Stuart, J.; Colpitts, T.; Venkatasubramanian, R. *Appl. Phys. Lett.* **2005**, *87*, 023105.
(23) Kanatzidis, M. G. *Chem. Mater.* **2010**, *22*, 648.
(24) Sootsman, J. R.; Chung, D. Y.; Kanatzidis, M. G. *Angew. Chem., Int. Ed.* **2009**, *48*, 8616.
(25) Lan, Y. C.; Minnich, A. J.; Chen, G.; Ren, Z. F. *Adv. Funct. Mater.* **2010**, *20*, 357.
(26) Dresselhaus, M. S.; Chen, G.; Tang, M. Y.; Yang, R. G.; Lee, H.; Wang, D. Z.; Ren, Z. F.; Fleurial, J. P.; Gogna, P. *Adv. Mater.* **2007**, *19*, 1043.
(27) Minnich, A. J.; Dresselhaus, M. S.; Ren, Z. F.; Chen, G. *Energy Environ. Sci.* **2009**, *2*, 466.
(28) He, J. Q.; Sootsman, J. R.; Xu, L. Q.; Girard, S. N.; Zheng, J. C.; Kanatzidis, M. G.; Dravid, V. P. *J. Am. Chem. Soc.* **2011**, *133*, 8786.
(29) Johnsen, S.; He, J. Q.; Androulakis, J.; Dravid, V. P.; Todorov, I.; Chung, D. Y.; Kanatzidis, M. G. *J. Am. Chem. Soc.* **2011**, *133*, 3460.
(30) Mi, J. L.; Zhao, X. B.; Zhu, T. J.; Tu, J. P. *Appl. Phys. Lett.* **2007**, *91*, 172116.
(31) Zide, J. M. O.; Vashaee, D.; Bian, Z. X.; Zeng, G.; Bowers, J. E.; Shakouri, A.; Gossard, A. C. *Phys. Rev. B* **2006**, *74*, 205335.
(32) Sootsman, J. R.; Kong, H.; Uher, C.; D'Angelo, J. J.; Wu, C. I.; Hogan, T. P.; Caillat, T.; Kanatzidis, M. G. *Angew. Chem., Int. Ed.* **2008**, *47*, 8618.
(33) Culp, S. R.; Poon, S. J.; Hickman, N.; Tritt, T. M.; Blumm, J. *Appl. Phys. Lett.* **2006**, *88*, 042106.
(34) Culp, S. R.; Simonson, J. W.; Poon, S. J.; Ponnambalam, V.; Edwards, J.; Tritt, T. M. *Appl. Phys. Lett.* **2008**, *93*, 022105.
(35) Maji, P.; Takas, N. J.; Misra, D. K.; Gabrisch, H.; Stokes, K.; Poudeu, P. F. P. *J. Solid State Chem.* **2010**, *183*, 1120.
(36) Sakurada, S.; Shutoh, N. *Appl. Phys. Lett.* **2005**, *86*, 082105.
(37) Shen, Q.; Chen, L.; Goto, T.; Hirai, T.; Yang, J.; Meisner, G. P.; Uher, C. *Appl. Phys. Lett.* **2001**, *79*, 4165.
(38) Yang, J.; Meisner, G. P.; Chen, L. *Appl. Phys. Lett.* **2004**, *85*, 1140.
(39) Uher, C.; Yang, J.; Hu, S.; Morelli, D. T.; Meisner, G. P. *Phys. Rev. B* **1999**, 8615.
(40) Yu, C.; Zhu, T. J.; Shi, R. Z.; Zhang, Y.; Zhao, X. B.; He, J. *Acta Mater.* **2009**, *57*, 2757.
(41) Chen, L. D.; Huang, X. Y.; Zhou, M.; Shi, X.; Zhang, W. B. *J. Appl. Phys.* **2006**, *99*, 064305/1.
(42) Yu, C.; Zhu, T.-J.; Xiao, K.; Shen, J.-J.; Yang, S.-H.; Zhao, X.-B. *J. Electron. Mater.* **2010**, *39*, 2008.
(43) Joshi, G.; Yan, X.; Wang, H.; Liu, W.; Chen, G.; Ren, Z. *Adv. Energy Mater.* **2011**, *1*, 643.
(44) Takas, N. J.; Sahoo, P.; Misra, D.; Zhao, H. F.; Henderson, N. L.; Stokes, K.; Poudeu, P. F. P. *J. Electron. Mater.* **2011**, *40*, 662.
(45) Makongo, J. P. A.; Misra, D. K.; Salvador, J. R.; Takas, N. J.; Wang, G.; Shabetai, M. R.; Pant, A.; Paudel, P.; Uher, C.; Stokes, K. L.; Poudeu, P. F. P. *J. Solid State Chem.* **2011**, *184*, 2948−2960.
(46) Makongo, J. P. A.; Misra, D. K.; Salvador, J.; Takas, N.; Stokes, K.; Gabrisch, H.; Poudeu, P. F. P. *Mater. Res. Soc. Symp. Proc.* **2010**, *1267*, DD05/11.
(47) Faleev, S. V.; Leonard, F. *Phys. Rev. B* **2008**, *77*, 214304.
(48) Uher, C.; Yang, J.; Meisner, G. P. In *18th International Conference on Thermoelectrics*; IEEE: Piscataway, NJ, 1999; Vol. 99TH8407, p 56.